Nanoscale

Accepted Manuscript

Cite this: DOI: 10.1039/c0xx00000x

www.rsc.org/xxxxxx

Paper

Improved Electron Transfer and Plasmonic Effect in Dye-sensitized Solar Cells with Bi-functional Nb-doped TiO_2/Ag Ternary Nanostructures

Jung Tae Park,[a] Won Seok Chi,[a] Harim Jeon,[a] and Jong Hak Kim[a,*]

Received (in XXX, XXX) Xth XXXXXXXXX 20XX, Accepted Xth XXXXXXXXX 20XX
DOI: 10.1039/b000000x

TiO_2 nanoparticles are surface-modified via atom transfer radical polymerization (ATRP) with a hydrophilic poly(oxyethylene) methacrylate (POEM), which can coordinate to the Ag precursor, i.e. silver trifluoromethanesulfonate ($AgCF_3SO_3$). Following application of the reduction of Ag ions, a Nb_2O_5 doping process and calcination at 450 °C, bi-functional Nb-doped TiO_2/Ag ternary nanostructures are generated. The resulting nanostructures are characterized by energy-filtering transmission electron microscopy (EF-TEM), X-ray diffraction (XRD), X-ray photoelectron spectroscopy (XPS), and UV-visible spectroscopy. The dye-sensitized solar cell (DSSC) based on the Nb-doped TiO_2/Ag nanostructure photoanode with a polymerized ionic liquid (PIL) as the solid polymer electrolyte show an overall energy conversion efficiency (η) of 6.9 %, which is much higher than those of neat TiO_2 (4.7 %) and Nb-doped TiO_2 (5.4 %). The enhancement of η is mostly due to the increase of current density, attributed to the improved electron transfer properties including electron injection, collection, and plasmonic effects without the negative effects of charge recombination or problems with corrosion. These properties are supported by intensity modulated photocurrent/voltage spectroscopy (IMPS/IMVS) and incident photon-to-electron conversion efficiency (IPCE) measurements.

1. Introduction

As requirements for renewable energy increase, new types of solar cell technologies have been attracting attention. In this regard, dye-sensitized solar cells (DSSCs) have been considered as promising alternatives to conventional silicon-based solar cells for transferring clean, inexhaustible sunlight into electricity due to their low manufacturing costs and relatively high energy conversion efficiencies.[1] During illumination of the DSSCs, electrons are injected from the photoexcited dye sensitizer into the conduction band of the wideband gap metal oxide (*e.g.* TiO_2), from which the electrons diffuses through the metal oxide layer and are then collected by a transparent conductive oxide (TCO) substrate. The oxide dye is regenerated via reduction by a redox electrolyte of I^-/ I_3^-. The oxidized form of the redox electrolyte diffuses to the counterelectrode and completes the circuit to generate a photocurrent. Research on DSSCs has been focused on achieving a higher energy conversion efficiency based on the design of suitable photoanode structures,[2-5] the synthesis of new dye sensitizers,[6-8] the preparation of electrochemically stable counterelectrodes,[9-11] and the fabrication of optimized ion transport electrolytes.[12,13] However, further improvements of device performance still remain an active area of technological research.

The wideband gap metal oxide layer is a key element because this layer performs multi-functions: (1) it serves as a substrate on which the dye sensitizers adsorb, (2) it transfers the electrons, and (3) it acts as a diffusion passage for redox electrolytes. In this regard, one way to successfully enhance the chemical and electronic properties is to introduce multi-functional doping species within the photoanode structure, such as niobium (Nb). This approach has the beneficial effect of enhancing electron transport properties such as enhanced electron injection and collection in the devices, which could further improve the short circuit current density (J_{sc}). In addition, the conduction band edge potential (E_{cb}) difference of Nb_2O_5 is approximately 100 mV more negative than that of TiO_2. This potential difference can form an energy barrier at the electrode/electrolyte interface, leading to a decrease in the rate of charge recombination and electron back reaction loss, thus enhancing the open-circuit voltage (V_{oc}). For example, the Huang group [14] developed a Nb-doped TiO_2 photoanode with enhanced electron transport properties for DSSC applications, which was further extended by other research groups.[15-17] Thus, to address this issue, the construction of a Nb-doped TiO_2 photoanode is a feasible and effective approach.

Another approach is to incorporate metal nanoparticles such as silver (Ag) and gold (Au) into the photoanode structure for improved chemical and electronic properties, *e.g.* the plasmonic

effect. Localized surface plasmon resonance from metal nanopaticles can excite dye sensitizers more efficiently than incident far field light, and thus the metal nanopaticles function as light-harvesting antennae for dye sensitizers with minimal impact on other material properties.[18-24] Despite the improved cell performance in the plasmon-enhanced DSSCs, the metal nanoparticles could potentially lead to problems such as increased charge recombination, the back reaction of photogenerated carriers, and detrimental corrosion caused by direct contact with the dye and the electrolyte, which would result in a lower Voc. To tackle this problem, core-shell structures have been applied which could inhibit the charge recombination, back reaction, and detrimental corrosion at the interface of the metal nanoparticles and dye/electrolyte.[18,19] The Snaith group presented an effective fabrication route for plasmon-enhanced DSSCs based on the $Au@SiO_2$ nanoparticle as a chemical additive.[18] In addition, the Hammond and Belcher groups have demonstrated an enhanced plasmon effect in DSSCs and reported energy conversion efficiencies (4.4 % at 100 mW/cm^2 for liquid electrolyte) much greater than those without core-shell $Ag@TiO_2$ nanoparticles.[19] Nevertheless, more conventional fabrication approaches (e.g. all-in-on photoanode systems or bi-functional plasmon enhanced solar cells) remain technologically important due to their possible solar cell applications. Therefore, a systematic study is needed to clarify multi-functional doping in tandem with the plasmon effect on the chemical and electronic structure of the nanocrystalline TiO_2 photoanode and its impact on the performance of photovoltaic devices.

DSSCs based on a nanocrystalline TiO_2 layer as a photoanode have reached efficiency levels of 12.3 %.[25] In addition, for the continuous enhancement of cell performance and stability, a fundamental understanding of the optimized ion transport electrolytes is necessary. For this purpose, solid-state or quasi-solid-state DSSCs are believed to have superior long-term stability and thus have been considered as alternatives to liquid electrolyte-based DSSCs. Recently, the Kanatzidis group reported a high efficiency of 8.5% by using $CsSnI_3$ perovskite as a hole conductor.[26] Additionally, the independent Snaith and Park groups achieved high efficiencies of 10.9% and 9.7 %, respectively, by using methyl ammonium lead iodide [$(CH_3NH_3)PbI_3$] and 2,2',7,7'-tetrakis-(N,N-di-p-methoxyphenylamine) 9,9'-spirobifluorene (spiro-MeOTAD) as the light harvester and hole conductor, respectively.[27,28] Our group also reported high efficiencies of 7.4% and 7.5 % based on a graft copolymer-directed TiO_2 photoanode and ionic liquid (IL)-grafted alumina (Al_2O_3) nanoparticles, respectively.[29,30]

In this work, bi-functional ternary nanostructures consisting of a TiO_2 core, Ag dot, and Nb_2O_5 shell were synthesized via atom transfer radical polymerization (ATRP), selective Ag reduction, and a doping process. The resultant nanostructures were used as a photoanode in DSSCs and characterized in detail by energy-filtering transmission electron microscopy (EF-TEM), X-ray diffraction (XRD), X-ray photoelectron spectroscopy (XPS), and UV-visible spectroscopy. The electrochemical and photovoltaic properties in DSSCs were characterized using intensity-modulated photocurrent/voltage spectroscopy (IMPS/IMVS), and incident photon-to-current conversion efficiency (IPCE). Particular attention was paid to two kinds of electrolytes for the fabrication of DSSC: (1) solid-state polymerized ionic liquid (PIL), i.e., poly(1-((4 ethenylphenyl)methyl)-3-butyl-imidazolium iodide) (PEBII); and 2) liquid electrolyte consisting of 1-butyl-3-methylimidazolium iodide, iodine (I_2), guanidinium thiocyanate, and 4-tert-butylpyridine (TBP) in acetonitrile and valeronitrile. To the best of our knowledge, there has been no report on such a bi-functional ternary nanostructure for DSSC applications.

2. Results and Discussion

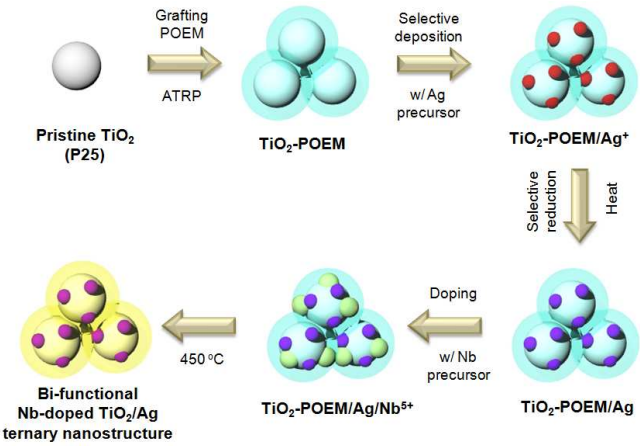

Fig. 1 Schematic representation of the preparation route for the bi-functional Nb-doped TiO_2/Ag ternary nanostructure via three steps.

Fig. 1 shows the preparation of the bi-functional Nb-doped TiO_2/Ag ternary nanostructure *via* subsequent ATRP, selective reduction, and a doping process. The morphological changes in three materials, i.e. pristine TiO_2, TiO_2-POEM, and the bi-functional Nb-doped TiO_2/Ag ternary nanostructure, were characterized by EF-TEM analysis, as shown in Fig. 2. EF-TEM has been demonstrated to be a very versatile and powerful tool for surface imaging at the nanometer scale of inorganic and organic materials. The spherical shape and relative uniform size (approximately 30 nm) of the pristine TiO_2 could be observed by the EF-TEM micrographs (Fig. 2a). Upon combining pristine TiO_2 with hydrophilic poly(oxyethylene) methacrylate (POEM) *via* the ATRP process, the morphology of the TiO_2-POEM was changed to an interconnected structure with a polymer shell of a thickness of below 10 nm (Fig. 2b), which indicates the formation of the interactive coordination seed sites for the next step, *i.e.* selective Ag nanoparticle reduction and the Nb doping process. In addition, the EF-TEM images of the TiO_2-POEM indicated that the addition of the hydrophilic polymer (POEM) has no obvious influence on the TiO_2 crystallite size compared to the pristine TiO_2. Upon the introduction of $AgCF_3SO_3$ as a Ag precursor and subsequent selective reduction by heat, followed by the doping process with $Nb(OCH_2CH_3)_5$ as a Nb-doped precursor and calcination at 450 °C, a bi-functional Nb-doped TiO_2/Ag ternary nanostructure (shell/core/dot) was generated (Fig. 2c). The corresponding high magnification EF-TEM image of Nb-doped TiO_2/Ag ternary nanostructure was also provided in Fig. S1. Viewing the morphological characteristics of the bi-functional ternary nanostructure, Ag nanoparticles (dot) with a diameter of 8 to 12 nm were homogeneously distributed over the pristine TiO_2

(core) nanoparticles surface and at the borders where the Nb-doped (shell) was seated.

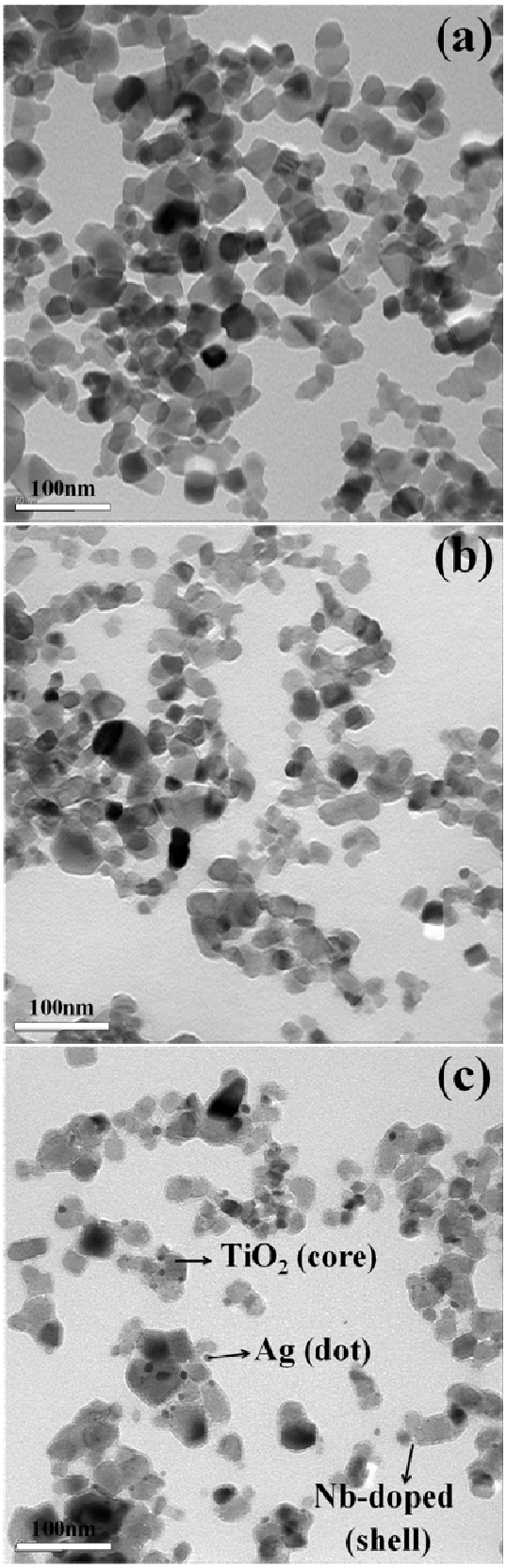

Fig. 2 EF-TEM micrographs of (a) pristine TiO_2, (b) TiO_2-POEM, and (c) the bi-fuctional Nb-doped TiO_2/Ag ternary nanostructure.

The use of Ag nanoparticles below 10 nm diameter in photoanode has shown to be more effective to enhance the performance of plasmonic DSSC. Similar structure consisting of Ag nanoparticles with diameters ranging from 3 to 8 nm in the photoanode could lead to a 1.25 times higher increase in energy conversion efficiency.[31] According to the previous study,[23] the total number of Ag nanoparticles can be determined by

$$\text{total number of Ag nanoparticles} = \text{total number of moles / number of mole per Ag nanoparticles} = \text{concentration} \cdot \text{volume} / (4/3)\,\pi r^3 \cdot \rho / M_w \quad (1)$$

herein, r is the radius of the Ag nanoparticle, ρ is the density, and M_w is the atomic weight.[23] Using this relation, the density of Ag nanoparticles in Nb-doped TiO_2/Ag ternary nanostructure was determined to be 5.3×10^{14} cm^{-3}.

It could be seen that the coating of the Nb-doped shell was uniform and continuous on the pristine TiO_2 nanoparticles surface with approximately 5 nm thickness. As mentioned in the introduction, there are several possible mechanisms by which the bi-functional Nb-doped TiO_2/Ag ternary nanostructure can cause an improvement of cell performance relating to the characteristics gained by selective Ag reduction and Nb-doping. First, the enhanced localized surface plasmon resonance effect of Ag nanoparticles in ternary nanostructures would be capable of greatly increasing the effectiveness of dye materials to harvest photons. It is well-known that when incident light excites the coherent oscillation of the free electrons of metal nanoparticles such as Ag or Au, it creates a collective oscillation of the conduction electrons called a plasmon, leading to an enhanced electromagnetic field that can then be coupled to the photoactive absorption region. In this context, the enhanced plasmon excitation of the Ag nanoparticles in the bi-functional Nb-doped TiO_2/Ag ternary nanostructure would increase the optical density of incoming light and improve the chance for dye molecules to generate photocurrents in the photoanode over a broad range of visible wavelengths.

Second, a wide band gap material (*i.e.* the Nb-doped shell) serving as an effective energy barrier at the photoanode/dye/electrolyte interface in the ternary nanostructure would energetically prevent the recombination process and delay the electron back reaction to provide a synergistic effect on cell performance. From the viewpoint of DSSC operations, irradiation of the dye molecules promotes the ground state to an excited state. Subsequently, the excited dye molecule transfers an electron diffusely through the photoanode toward the conducting substrate, although the longer the electrons spend in the photoanode, the higher the probability of their undergoing a recombination process before being collected, which often limits V_{oc}. In this regard, the Nb-doped shell coating layer in the bi-functional ternary nanostructure would form an efficient energy barrier at the photoanode/dye/electrolyte interface, which suppresses the electron recombination process and is expected to enhance the V_{oc} in DSSCs. Since the conduction band potential of the Nb-doped shell is approximately 100 meV negative of the potential of the TiO_2 core, the electrons would facilitate injection into the electrodes; *i.e.*, the electrons will favor the material having the more positive conduction band. A detailed discussion on the

correlation between the electron recombination process and V_{oc} in DSSCs can be found in the following analysis. In addition, when an energy barrier (Nb-doped shell coating layer) is formed at the surface of the ternary nanostructure, it is possible to not only reduce interfacial recombination but also improve electron transfer including electron injection (η_{inj}) and collection efficiency (η_{cc}) in the DSSCs, thus increasing its J_{sc} with respect to a control group. This expectation is in good agreement with what was seen in the IPCE spectrum of the bi-functional Nb-doped TiO_2/Ag ternary nanostructure.

Third, the Nb-doped shell layer in the ternary nanostructure also would have a beneficial effect on electron mobility due to facile electron transport during device operation. According to previous research about electron transfer characteristics at the photoanode and electrolyte interface, smaller effective electron mass (m^*) leads to beneficial effects on electron mobility (μ) in DSSCs.[32,33] Therefore, we can expect that a wide band gap material such as Nb_2O_5 in the ternary nanostructure gives rise to a smaller effective electron mass (m^*) compared to the control group, leading to improved electron mobility (μ) characteristics. Narrow band gap material such as TiO_2 provides a high effective electron mass (m^*) value (~10 and 50 m_e), whereas wide band gap material such as Nb_2O_5 possesses a low effective electron mass (m^*) value (4 m_e).[32,33] In addition, the electrical conductivity in DSSCs is related to the electron transfer ability at the photoanode and electrolyte interface according to:

$$\sigma = n \cdot e \cdot \mu \quad (2)$$

where n denotes the concentration of electrons, e is the elementary charge, and μ is the electron mobility. Considering that the concentration of electrons (n) and elementary charge (e) in the photoanode and electrolyte interface is constant under our experimental conditions, the relation between electrical conductivity (σ) and the electron mobility (μ) can be expressed as a linear function. Therefore, the Nb-doped shell layer in the bi-functional ternary nanostructure suggests that the enhanced overall mobility of the excited electrons is related to the conductivity, which results in the enhancement of electron transport through the photoanode in DSSCs. Because the improved electron conductivity strongly influences the facile electron transport properties of the polycrystalline photoanode, it plays an important role in device applications. In addition, our suggestions about the relationship between electron transport and cell performance are consistent with a previous study by the Huang group which suggests that the change of J_{sc} was affected by electron transport in the photoanode network.[14] The Nb-doped shell layer plays a pivotal role in not only protecting the plasmonic metal Ag nanoparticles from corrosion by the electrolyte but also inhibiting the charge trapping between metal (Ag) and semiconductor (TiO_2), which is related to the recombination and back reaction of photogenerated carriers. Similar structures consisting of plasmonic nanoparticles@metal oxides core-shell were employed to enhance cell performance without detrimental side effects on charge recombination.[19,20,34] As previously stated, the effect of the selective Ag nanoparticles reduction and Nb doping process on photovoltaic parameters such as an enhanced plasmon effect, energy barrier, and facile electron transport are closely related to the alteration of the characteristic structure of the photoanode. Hence, these issues will be intensively discussed in the next section. In particular, in the subsequently outlined electrochemical studies such as IMPS and IMVS, this method proved to be sufficient for preventing Ag nanoparticles corrosion by the surrounding electrolyte.

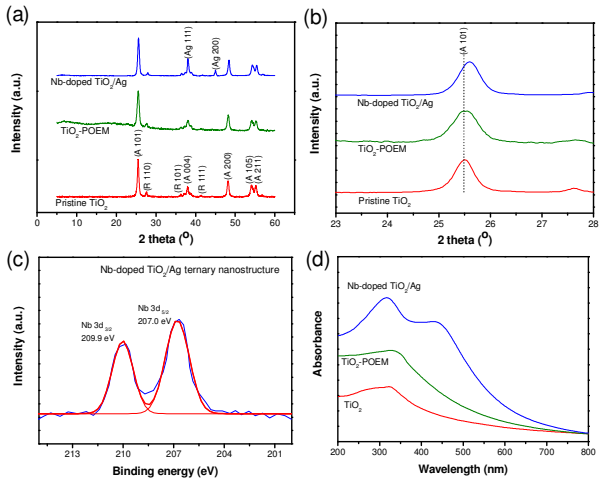

Fig. 3 XRD patterns of pristine TiO_2, TiO_2-POEM, and the bi-functional Nb-doped TiO_2/Ag ternary nanostructure; (a) whole range and (b) narrow range. Anatase phase TiO_2 and Ag nanoparticles are denoted by A and Ag, respectively, based on the ICDD-JCPDS card for anatase phase TiO_2 (no. 86–1157) and Ag (no. 04-0783), respectively. (c) XPS profiles of Nb 3d regions for the bi-functional Nb-doped TiO_2/Ag ternary nanostructure, (d) UV-visible absorption spectra of TiO_2, TiO_2-POEM, and the bi-functional Nb-doped TiO_2/Ag nanostructure in deionized water.

Structural changes of the bi-functional Nb-doped TiO_2/Ag ternary nanostructure was investigated using XRD analysis, as shown in Fig. 3a. In particular, the enlarged pattern of the peak corresponding to (101) planes of anatase phase TiO_2 was presented in Fig. 3b. The peak locations and relative intensities for TiO_2 and Ag are cited from the Joint Committee on Powder Diffraction Standards (JCPDS) database. The pristine TiO_2 nanoparticles exhibited well-developed diffraction peaks centered at 2θ = 25.5, 37.9, 48.2, 54.3, and 55.2 °, which corresponded to the (101), (004), (200), (105), and (211) reflections, respectively, of the anatase phase TiO_2 (ICDD-JCPDS, No. 86–1157). There was also a small portion of rutile phase in the pristine TiO_2 (P25), as can be seen in the small diffraction peaks at 2θ = 27.6, 36.4, and 41.2 °, assigned to the (110), (101), and (111) reflections, respectively. After the ATRP process of POEM to the pristine TiO_2, two broad peaks with weak intensity appeared at 7.2 and 17.6 ° which were attributed to the amorphous flexible molecular structures of the POEM chains.[35] In addition, the TiO_2-POEM exhibited several sharp crystalline anatase phase TiO_2 peaks with similar position and crystallinity as the pristine TiO_2, suggesting that the crystalline structure of the TiO_2 nanoparticles was not significantly altered by the polymer grafting. Thus, the POEM shell layer not only functions as interactive coordination seed sites for the following selective reduction and doping process, but also protects the TiO_2 cores from reacting with the aggregates to form larger TiO_2 particles. The selective Ag reduction and Nb doping process have three remarkable effects on the structure of Nb-doped TiO_2/Ag. First, upon the introduction of the Ag

precursor in TiO_2-POEM and subsequent selective reduction by heating, two additional peaks at 2θ values of 38 and 44 ° appeared that were assigned to the (111) and (200) Bragg's reflections, respectively, of the face-centered cubic structure of metallic Ag (ICDD-JCPDS Ag, No. 04-0783). This result clearly reveals the presence of highly crystalline metallic Ag nanoparticles anchored on the surfaces of the Nb-doped TiO_2/Ag ternary nanostructure without preferred orientations. In addition, this observation suggests that the Ag nanoparticles in the ternary nanostructure can endure thermal treatment without detachment, which is essential in fabricating the photoanode of DSSCs. Second, contrary to our expectation, we could not see any crystalline characteristic peaks of niobium oxide in the Nb-doped TiO_2/Ag ternary nanostructure. These XRD results can be explained by the fact that amorphous state niobium oxide can be crystallized to a pseudo-hexagonal Nb_2O_5 at a temperature of at least 600 °C.[36] In other words, the crystallization process of niobium oxide certainly did not occur at 450 °C, which was chosen as the calcination temperature in this study. On the other hand, from an enlarged version of the XRD pattern (Figure 3b), one can see that the maximum peak position for the anatase phase TiO_2 (101) plane shifted to a higher 2θ value by approximately 0.1°, indicating the change of *d*-spacing due to epitaxial growth of the amorphous-state niobium oxide on the TiO_2 matrix. The value of *d*-spacing can be calculated from the peak maximum using Bragg's Law (3):

$$n\lambda = 2d \cdot \sin\theta \quad (3)$$

where *n* is the positive integer, λ is the wavelength (1.5406 Å), *d* is the inter-planar distance, and θ is the angle from the crystal plane.[37] According to the above Bragg relation, the inter-segmental *d*-spacing values of the pristine TiO_2 and bi-functional Nb-doped TiO_2/Ag ternary nanostructure were determined to be 3.49 and 3.47 Å, respectively. The decrease of *d*-spacing is presumably attributable to compressive strain, which arises from the differences in the bonding characteristics between niobium and oxygen. A similar effect in the Nb-doping on the TiO_2 phase transformation was reported by Chen et al.[38] Third, the halo pattern of amorphous POEM chains was not detected for the Nb-doped TiO_2/Ag, indicating the complete removal of organic polymers *via* the calcination process at 450 °C. Therefore, these results support the assertion that the calcination process not only decomposes the organic material POEM (shell) from the surface of TiO_2 (core) nanoparticles, but also completely replaces the coordination seed sites POEM (shell) with the doped Nb (shell). These XRD results were also supported by the Nb 3d XPS spectra for the bi-functional Nb-doped TiO_2/Ag ternary nanostructure, as shown in Fig. 3c. Two distinct peaks were observed with binding energies of 207.0 and 209.9 eV, corresponding to the binding energy of the Nb $3d_{5/2}$ and $3d_{3/2}$ peaks, respectively. The binding energy difference of 2.9 eV corresponds to the Nb 3d level splitting, which is consistent with the previously reported values.[39] Accordingly, these XPS peaks indicate that the doped Nb (shell) was incorporated into the TiO_2 lattice. The weight ratio of TiO_2, Nb and Ag was approximately 11.1:1.3:1, as determined by XPS analysis.

For the purpose of further investigating the influence of selective Ag reduction and Nb doping process in the TiO_2-POEM template, UV-visible absorption spectra was used to study the chemical alternations of the TiO_2 surfaces, as shown in Fig. 3d. The onset of absorption allows us to calculate the E_g (band gap energy) value for TiO_2 nanoparticles by using the Planck's equation (4):

$$E_g = h \cdot c / \lambda = 1240 / \lambda \quad (4)$$

where E_g is the band gap energy (eV), *h* is Planck's constant, *c* is the velocity of light (m/s), and λ is the wavelength (nm). UV-visible absorption spectra of pristine TiO_2 nanoparticles exhibited a broad absorption peak at 330nm, attributed to the presence of polytitanium $(Ti–O–Ti)_n$ clusters in the bulk state of TiO_2.[40] The E_g value of pristine TiO_2 was estimated to be 3.14 eV, according to the Planck equation. Upon graft polymerization of POEM to pristine TiO_2, a more broad and slightly red-shifted UV-visible absorption peak at around 300~330 nm was observed, probably related to the modification in the surface properties of TiO_2 nanoparticles.[41] Following the selective Ag reduction and Nb doping process in the TiO_2-POEM template, two significant characteristic absorption peaks could be seen in the bi-functional Nb-doped TiO_2/Ag ternary nanostructure. Upon the introduction of the Nb precursor to TiO_2-POEM for the doping process, the onset of absorption was shifted slightly to a shorter wavelength (from 395 to 387nm) compared to the pristine TiO_2. This result reveals that the Nb doping process in TiO_2-POEM changes the chemical environment in the TiO_2 surface, that is, a small increase of band gap energy when Nb is in interstitial positions. The E_g value of the Nb-doped TiO_2/Ag ternary nanostructure was calculated to be 3.20 eV, which is slightly higher than that of pristine TiO_2. From this result, we can anticipate that the presence of the Nb shell layer in the Nb-doped TiO_2/Ag ternary nanostructure will provide a positive effect on cell performance in terms of V_{oc}. A negative shift in the conduction band edge potential (E_{cb}) of TiO_2 for the Nb-doped TiO_2/Ag ternary nanostructure may increase the energy gap between the Fermi level (V_{fb}) and the potential of the I^-/I_3^- redox species in the electrolyte (V_{red}), resulting in V_{oc}. Theoretically, under illumination, the V_{oc} value are estimated from the equation (5)

$$V_{oc} = \left| V_{fb} - V_{red} \right| \quad (5)$$

where V_{fb} is the potential of the Fermi level and V_{red} is the standard reduction potential of a redox couple.[42] Assuming that V_{red} does not vary with the addition of Nb into the TiO_2-POEM and that V_{fb} is located near the E_{cb}, it is expected that the V_{oc} depends on the V_{fb}, which is related to the E_{cb} position. Therefore, it is expected that the introduction of Nb into the TiO_2-POEM results in the enhancement of V_{oc} by not only decreasing the charge recombination and the electron back reaction at the phoroanode/dye/electrolyte interface (energy barrier effect, as shown in the introduction), but also the higher E_{cb} with respect to the vacuum as compared to the control group (increased absolute value between the V_{fb} and the V_{red}). In addition, the Nb doped layer in the ternary nanostructure will prevent direct contact of the corrosive I^-/I_3^- electrolyte with the Ag nanoparticles, resulting

in suppressed corrosion during DSSC operations. Second, upon the introduction of an Ag precursor to the TiO_2-POEM and subsequent selective reduction by heating, the Nb-doped TiO_2/Ag ternary nanostructure showed a dramatic increase in the absorption spectrum in the visible range with the appearance of a broad peak ranging from 400 nm to 460 nm, which is attributed to the plasmon resonance absorption peak arising from the Ag nanoparticles.[43] Compared with the UV-vis absorption spectra of Ag nanoparticles based on polymer templates in our earlier reports,[43,44] the absorption peak of the Nb-doped TiO_2/Ag ternary nanostructure exhibited a red shift to 460 nm, which is due to the higher refractive index surrounding the Ag of inorganic material TiO_2 than that of the organic polymer template. Thus, we can expect that the improved plasmon excitation in the optical density of incoming light near the surface of the Ag nanoparticle in the ternary nanostructure is capable of significantly enhancing light harvesting efficiency, leading to the higher energy conversion efficiency of DSSCs.

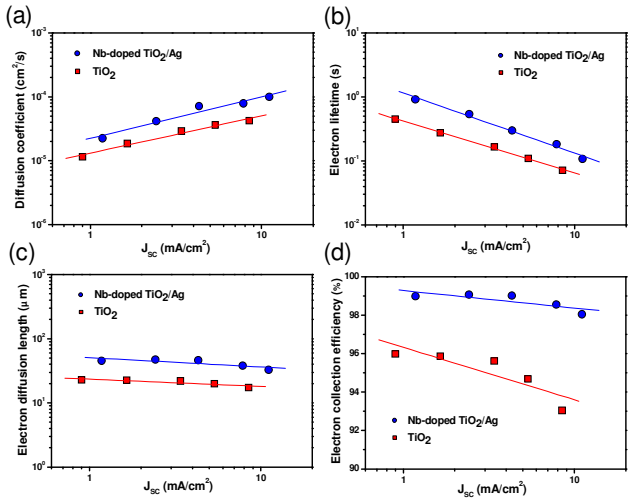

Fig. 4 (a) Diffusion coefficients (D_n), (b) electron lifetime (τ_r), (c) electron diffusion length (L_n), and (d) electron collection efficiency (η_{cc}) as a function of the *Jsc* for the two solid electrolyte DSSCs fabricated from pristine TiO_2 and the Nb-doped TiO_2/Ag ternary nanostructure photoanode measured by IMPS and IMVS.

The mechanism underlying the photovoltaic performance improvement in the bi-functional Nb-doped TiO_2/Ag ternary nanostructure was investigated by measuring the electron transport and charge recombination properties through IMPS and IMVS measurements. Diffusion coefficients (D_n), electron lifetime (τ_r), electron diffusion length (L_n), and electron collection efficiency (η_{cc}) results as a function of J_{sc} derived from IMPS and IMVS measurements are shown in Fig. 4a, b, c, and d, respectively. The D_n and τ_r in the Nb-doped TiO_2/Ag nanostructure can be obtained by fitting the frequency-dependent response using the following analytical relations:

$$\tau_t = 1/2\pi f_t \quad (6) \qquad D_n = d^2/2.35\tau_t \quad (7)$$
$$\tau_r = 1/2\pi f_r \quad (8)$$

where f_t is the characteristic frequency at the minimum of the imaginary component of the IMPS result, τ_t is the electron transport time, d is the thickness of the photoanode, and f_r is the characteristic frequency at the minimum of the imaginary component of the IMVS result. The competition between the transport and recombination of electrons is reflected in the L_n and η_{cc} in the Nb-doped TiO_2/Ag nanostructure, which can be expressed as:

$$L_n = (D_n \tau_r)^{1/2} \quad (9)$$
$$\eta_{cc} = 1 - \tau_t/\tau_r \quad (10)$$

where D_n is the diffusion coefficient, τ_r is the electron lifetime, and τ_t is the electron transport time in the previous IMPS and IMVS analysis.[45-47]

Fig. 4a shows that the D_n values of the Nb-doped TiO_2/Ag-based DSSC are always greater than those of the pristine TiO_2 over the light intensity ranges. Furthermore, the τ_r and L_n values of the Nb-doped TiO_2/Ag-based cell were greater than those of the pristine TiO_2-based cell, as shown in Fig. 4b and c. This significant improvement of electron transport and reduced charge recombination in the bi-functional Nb-doped TiO_2/Ag ternary nanostructure can be understood by examining two basic causes. The first reason is related to the enhanced mobility and conductivity of the Nb-doped TiO_2/Ag nanostructure arising from the smaller effective electron mass within the Nb-doped shell, resulting in improved electron transport for a longer distance with less diffusive hindrance. The second is associated with the wide band gap material Nb-doped shell in the bi-functional ternary nanostructure, which can afford an effective energy barrier at the photoanode/dye/electrolyte interface to reduce the possibility of electron trapping for charge recombination and electron back reaction while enhancing the electron injection efficiency (η_{inj}). In addition, under the illumination state, the V_{oc} related to the recombination or back reactions occurring at the photoanode and electrolyte interface can be described with the following equation:

$$V_{oc} = (RT/nF) \cdot ln\,(AI/(n_o k_1(I_3^-) + n_0 k_2(D^+))) \quad (11)$$

where R is the molar gas constant, T is the temperature, F is the Faraday constant, n is the reaction order for triiodide (I_3^-) and electrons, A is the electrode area, I is the incident photon flux, n_o is the concentration of accessible electron states in the conduction band, and k_1 and k_2 are the kinetic constants of the back reaction of the injected electrons with triiodide (I_3^-) and the recombination of these electrons with oxidized dyes (D^+), respectively.[49] Therefore, we can expect that V_{oc} will depend logarithmically on the inverse of the kinetic constant of the back reaction of the injected electrons with I_3^- (k_1) and the recombination of these electrons with D^+ (k_2). Accordingly, the reduced possibility of electron trapping for charge recombinations and electron back reactions of the Nb-doped TiO_2/Ag nanostructure implies that η_{inj} and V_{oc} can be enhanced by wide band gap material Nb-doped shells introduced as energy barriers in DSSCs. Furthermore, the η_{cc} is also a significant factor that directly influences cell performance since it is related to the competition between transport and the recombination of electrons. In Fig. 4d, we observed a higher η_{cc} in the Nb-doped TiO_2/Ag nanostructure-based DSSC compared to those of pristine TiO_2. In addition, the η_{cc} for Nb-doped TiO_2/Ag cells remained nearly constant under

various light intensities while a decreasing tendency in the η_{cc} was observed for pristine TiO_2 cells at high light illumination conditions, which leads to an enhanced J_{sc} of the Nb-doped TiO_2/Ag-based cells even at high illumination. In addition, it is noted that the exposed Ag nanoparticles on the TiO_2 nanoparticles are insulated from the electrolyte via the Nb-doped shell, inhibiting the charge recombination on the Ag/electrolyte interface while not affecting the regeneration of the dye from the electrolyte. The dye loading was not significantly different among TiO_2, Nb-doped TiO_2 and Nb-doped TiO_2/Ag ternary nanostructure (Fig. S2), indicating small effect of Nb-shell on the dye anchoring. Also, the long-term stability effect of Nb-shell on dye loading was not clear when measured after 7 days. However, the suppression of electron recombination process by the Nb shell was confirmed by EIS curves of DSSCs measured under dark condition (Fig. S3).

The localized electric fields by the plasmonic metal nanoparticles can excite dyes more effectively than the incident far field light for increased light harvesting efficiency. In addition, the enhancement of DSSC performance with energy barrier doping in the nanostructured photoanode is either associated with improved electron transport, the suppression of recombination, or the shift of the conduction band. Therefore, to reveal the effect of the plasmonic metal nanoparticle and the energy barrier doping in the nanostructured photoanode, the absolute IPCE as a function of wavelength for the devices composed of pristine TiO_2 and Nb-doped TiO_2/Ag ternary nanostructure photoanodes were measured and are shown in Fig. 5a. The IPCE is determined by the light harvesting efficiency of the sensitized TiO_2 photoanode (η_{lh}), the efficiency of electron injection from the excited sensitizer into the photoanode conduction band (η_{ijh}), and the electron collection efficiency of photo-generated charge carriers (η_{col}).[50] In particularly, the η_{lh} is related to the light management characteristic by a sensitizer. The other significant parameters include the η_{ijh}, and η_{col} associated with the cascading energy band matching, the electron diffusion coefficient (D_n), and the electron lifetime (τ_r). As can be seen in Fig. 5a, the DSSC using the Nb-doped TiO_2/Ag ternary nanostructure photoanode showed a better photoelectrical response, with an IPCE obviously higher than that of the pristine TiO_2-based device over the entire visible light wavelength range. Compared to the pristine TiO_2 device, the incorporation of the Nb-doped shell and Ag nanoparticle dot in the bi-functional ternary nanostructure device led to a 20 % increase in the IPCE around 525 nm. The improvement in IPCE value suggests that devices based on bi-functional ternary nanostructures have better η_{lh} and more η_{ijh} and η_{col} behavior than those of pristine TiO_2. η_{lh} can be increased by plasmon-enhanced light absorption by Ag nanoparticles, while ηinj, and η_{col} can be improved by Nb-doped shell surface treatment by effectively insulating the exposed Ag nanoparticles from the oxidized form of the electrolyte, as shown in previous IMPS/IMVS studies. Furthermore, the slight red shift of the IPCE spectra was observed for the DSSC with the Nb-doped TiO_2/Ag ternary nanostructure, which is due to the increase in the refractive index of the environment resulting from plasmonic coupling between the metal particles.[51] The increase of IPCE value was smaller than that of the overall absorption value, which is because the optimized thick photoanodes have little effect on photo-absorption in the strong absorption range of dye sensitizer,[23] as similar results were reported previously.[19,52] For example, the Hammond and Belcher group observed a slight increase in the IPCE value compared to the optical density when metal@oxide core-shell nanostructures were incorporated.[19] Also, the Lee group found that the increase of the optical density in plasmonic TiO_2/core-shell structure lead to slight enhancement of IPCE value.[52]

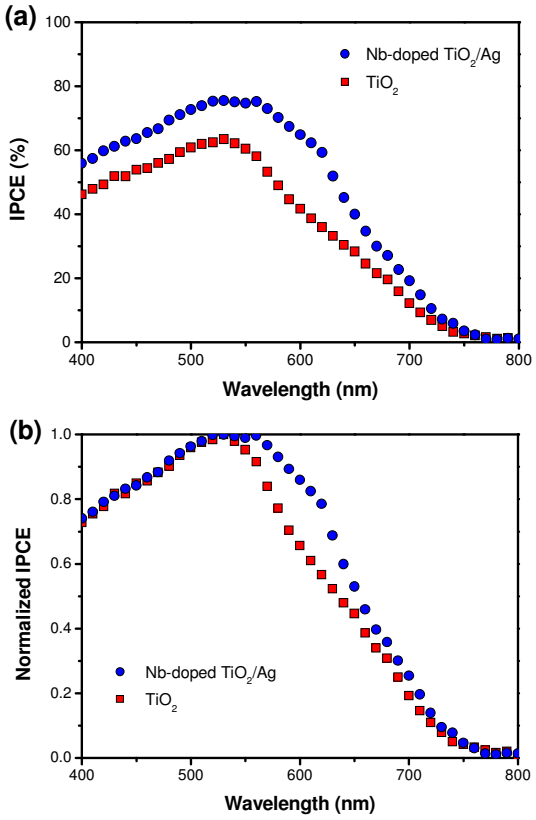

Fig. 5 (a) Absolute and (b) normalized IPCE spectra of the solid electrolyte DSSCs based on pristine TiO_2 and the Nb-doped TiO_2/Ag ternary nanostructure photoanode, and using a solid electrolyte of poly(1-((4ethenylphenyl)methyl)-3-butyl-imidazolium iodide)) (PEBII).

On the other hand, the spectrally-selective improvement of light harvesting is considerable in the normalized IPCE spectra for these two devices, as shown in Fig. 5b. Notably, the IPCE value of DSSCs based on Nb-doped TiO_2/Ag ternary nanostructures showed a significant broadening at 550~650 nm as compared with pristine TiO_2. Such broadening of the spectrum domain suggests increased light harvesting in this range, which is attributed to the enhanced plasmonic effect by the Ag nanoparticles in the ternary nanostructure which maximizes device performance. There was slight difference between the wavelength maximum in the IPCE spectra (with electrolyte, dye sensitizer) and the absorption peak with Ag nanoparticles in UV-visible spectroscopy (without electrolyte, dye sensitizer) for the Nb-doped TiO_2/Ag ternary nanostructure. The maximum peak position of IPCE was red-shifted from UV-vis absorption peak, which is due to optical interference of the Ag nanoparticles by the electrolyte and/or Ru based sensitizer in the Nb-doped TiO_2/Ag ternary nanostructure. Similarly, Hupp et al. observed a red shift

in the wavelength maximum in the IPCE spectra relative to absorption peak when Ag nanoparticles were introduced to enhance solar cell performance.[31] A significantly higher IPCE value at higher wavelength region could be related to the improved electron transfer properties of Nb-doped TiO_2/Ag ternary nanostructure. Kim et al. observed that TiO_2 nanoparticles functionalized with Nb exhibited an enhanced IPCE value in higher wavelength region than those of control group.[53]

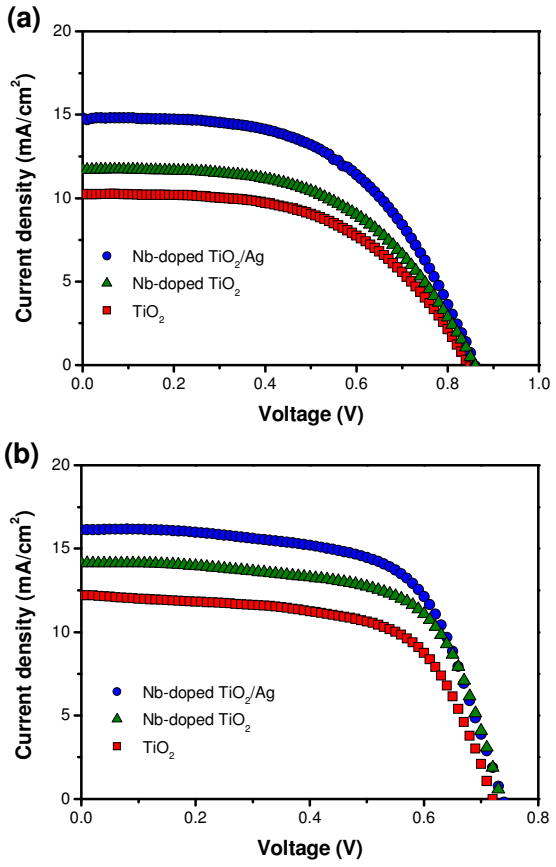

Fig. 6 *J-V* curves of DSSCs fabricated using pristine TiO_2, Nb-doped TiO_2, and the Nb-doped TiO_2/Ag ternary nanostructure at 100 mW/cm^2 upon using (a) a solid PEBII electrolyte and (b) a liquid electrolyte consisting of 1-butyl-3-methylimidazolium iodide, I_2, guanidinium thiocyanate, and 4-tert-butylpyridine in a mixture of acetonitrile and valeronitrile.

The performances of the Nb-doped TiO_2/Ag ternary nanostructure photoanodes were evaluated in DSSCs with N719 Ru-dye, a Pt-coated counterelectrode, and two types of electrolytes (solid and liquid type) under one sun (AM 1.5) illumination, as shown in Fig. 6. In addition, reference devices were fabricated using pristine TiO_2 and Nb-doped TiO_2 as the photoanode material. The device parameters including V_{oc}, J_{sc}, *FF*, and η are tabulated in Table 1 for easy comparison. The thickness of photoanode was approximately 7 μm. The solid electrolyte DSSCs fabricated with the pristine TiO_2 photoanode and the solid electrolyte showed η as low as 4.7%, mostly due to a lower J_{sc} value (10.2 mA/cm^2). After the surface of the photoanode was treated with Nb precursor (Nb-doped TiO_2), J_{sc} was increased to 11.7 mA/cm^2 with a similar FF of 0.54, while V_{oc} was slightly improved to 0.85 V. Subsequently, the η of the DSSC was improved to 5.4%. In particular, the J_{sc} was found to be highly improved for the DSSC with the Nb-doped TiO_2, attributable to the smaller effective electron mass (m^*) and the wide band gap characteristics of the Nb-doped shell structure, which could enhance electron transfer properties such as electron injection and collection in the DSSCs. Some possible contributions to the improved V_{oc} value include the reduced charge recombination, electron back reaction loss, and the raising of the E_{cb} of the photoanode by the Nb-doped shell structure. The increase of the E_{cb} of the photoanode by the Nb-doped shell structure was also characterized using optical absorption spectra (Fig. S4). The optical absorption spectra of the Nb-doped TiO_2 photoanode was slightly shifted to a shorter wavelength with a band gap transition. This result suggests that E_{cb} has a negative shift with Nb doping in the TiO_2 lattice, which is consistent with the results reported by Nikolay et al.[17] The V_{oc} of the Nb-doped TiO_2/Ag ternary nanostructure was similar to that of Nb-doped TiO_2, but the J_{sc} of the former (14.8 mA/cm^2) was 1.26 times higher than that of the latter (11.7 mA/cm^2). Thus, the η (6.9%) of the Nb-doped TiO_2/Ag ternary nanostructure was 28 % higher than that of the Nb-doped TiO_2 (5.4%), indicating the important role of Ag nanoparticles. It should be noted that a solid polymer electrolyte DSSC with 6.9 % efficiency at 100 mW/cm^2 is among the highest observed for N719 dye.[29,30,54-58] As previously discussed, the J_{sc} value was interpreted by correlating the IPCE with the light harvesting properties:

$$J_{sc} = q \cdot \eta_{IPCE} \cdot I_0 = q \cdot \eta_{lh} \cdot \eta_{inj} \cdot \eta_{col} \cdot I_0 \quad (12)$$

where q is the elementary charge, η_{IPCE} is the IPCE efficiency value, I_0 is the light flux, η_{lh} is the light harvest efficiency of a cell, η_{inj} is the electron injection efficiency, and η_{col} is the electron collection efficiency.[57] Therefore, the drastic improvement in J_{sc} comes from the increased η_{lh} by the plasmonic-enhanced Ag nanoparticles in the bi-functional ternary nanostructure, which leads to increased η values. In addition, it is noted that metallic nanoparticles such as Ag and Au are not only good plasmonic-enhanced materials, but also often serve as recombination sites for photogenerated charge carriers, which often limits V_{oc}. However, the Nb-doped shell in the bi-functional ternary nanostructure has a good affinity to Ag nanoparticles, effectively insulating the exposed Ag nanoparticle sites from the oxidized form of the electrolyte which could help prevent corrosion problems of metal nanoparticles. Therefore, the adsorption of the Nb-doped shell onto the exposed Ag nanoparticle sites substantially retards the charge recombination between the Ag nanoparticles and the electrolyte, leading to the effective utilization of the plasmonic effect without any side effects. Similar results were obtained in the DSSCs fabricated with liquid electrolytes in which iodine was used, as shown in Fig. 6b and Table 1. The Nb-doped TiO_2/Ag ternary nanostructure showed a smaller increase in V_{oc} than expected in the solid electrolyte DSSCs. In order to clearly investigate the Nb shell on V_{oc} values, the thickness of TiO_2 photoanode was increased from 7 to 14 μm, in which the overall V_{oc} values are reduced due to insufficient pore-infiltration of solid electrolyte (Fig. S5 and Table S1). The positive effect of the Nb shell on V_{oc} values was clearly observed for high thickness of TiO_2 photoanode. It is therefore concluded that a considerable efficiency enhancement in the DSSC fabricated with Nb-doped TiO_2/Ag ternary nanostructure photoanodes is due to the synergy of improved electron transfer

including electron injection and collection, and the plasmonic effect. The bi-functionalities of the Nb-doped TiO_2/Ag ternary nanostructures could suggest a new strategy for enhancing the performances of various photo-electrochemical devices.

Table 1 Photovoltaic properties of three types of DSSCs fabricated using TiO_2, Nb-doped TiO_2 and Nb-doped TiO_2/Ag ternary nanostructure with solid and liquid state electrolytes at 100 mW/cm^2. The thickness of electrode is approximately 7 μm.[a]

Photoanode	*Electrolyte*	V_{oc} (V)	J_{sc} (mA/cm^2)	*FF*	η (%)
TiO_2	Solid	0.84	10.2	0.54	4.7
	Liquid	0.71	12.2	0.64	5.5
Nb-doped TiO_2	Solid	0.85	11.7	0.54	5.4
	Liquid	0.73	14.1	0.65	6.8
Nb-doped TiO_2/Ag	Solid	0.85	14.8	0.55	6.9
	Liquid	0.73	16.1	0.64	7.6

[a] Solid electrolyte: poly(1-((4ethenylphenyl)methyl)-3-butyl-imidazolium iodide)), PEBII, Liquid electrolyte: 1-butyl-3-methylimidazolium iodide/I_2/guanidinium thiocyanate/4-tert-butylpyridine in acetonitrile and valeronitrile.

3. Conclusions

This study presents a novel method for the preparation of a bi-functional ternary nanostructure for DSSC applications with an Ag dot and Nb_2O_5 shell adsorbed onto the TiO_2 core. TiO_2 nanoparticles were surface-modified with hydrophilic POEM long chains, which can coordinate to Ag and Nb precursors via the ATRP process. Using a combination of selective reduction and doping processes, bi-functional Nb-doped TiO_2/Ag ternary nanostructures were prepared. The DSSCs based on the bi-functional Nb-doped TiO_2/Ag photoanodes showed higher efficiency than those with pristine TiO_2 or Nb-doped TiO_2. Upon using PEBII as a solid PIL electrolyte, a high energy conversion efficiency of 6.9 % at 100 mW/cm^2 could be achieved. The remarkable enhancement of the photovoltaic performance is mainly attributed to the improved electron transfer properties including electron injection, collection, and plasmonic effects without unintentionally introducing other complications such as an increased charge recombination or corrosion problems. We believe that research aiming to enhance light management in other solar cell devices can take advantage of this investigation.

4. Experimental Section

Materials

Commercial TiO_2 (P25) was purchased from Degussa, Germany. 2-Chloropropionyl chloride (CPC, >97%), triethylamine (TEA, >99.5%), 4-(dimethylamino) pyridine (DMAP, >99%), poly(oxyethylene methacrylate) (poly(ethylene glycol) methyl ether methacrylate, POEM, Mn = 475 g/mol), 1,1,4,7,10,10-hexamethyltriethylene-tetramine (HMTETA), copper(I) chloride (CuCl), silver trifluoromethanesulfonate ($AgCF_3SO_3$ >99%), niobium ethoxide ($Nb(OCH_2CH_3)_5$), titanium(IV) bis(ethyl acetoacetato) diisopropoxide, 1-butyl-3-methylimidazolium iodide, iodine (I_2), guanidinium thiocyanate, 4-tert-butylpyridine, sodium hydroxide (NaOH), 1-butylimidazole, 4-chloromethylstyrene, lithium iodide (LiI), ethyl acetate, magnesium sulfate ($MgSO_4$), and 2,2'-azobisisobutyronitrile (AIBN), and chloroplatinic acid hexahydrate (H_2PtCl_6) were purchased from Sigma-Aldrich. Methylene dichloride (MC, 99.8%), dimethyl sulfoxide (DMSO, 99.9%), acetonitrile (99.9%), butanol (99.9%), 2-propanol (99.9%), chloroform (99.9%), ethanol (99.9%), diethylether (99.9%), and valeronitrile were purchased from J.T. Baker. Deionized water (>18 MΩ·m) was obtained with a water purification system made by Millipore Corporation. Ruthenium dye (535-bisTBA, N719) and Surlyn (60 μm thick) were purchased from Solaronix, Switzerland. Fluorine-doped tin oxide (FTO)-conducting glass substrate (TEC8, 8 ohms/sq, 2.3 mm thick) was purchased from Pilkington, France. All the solvent and chemical reagents used in the experiments were obtained from commercial sources as guaranteed grade reagents and used without further purification.

Preparation of hybrid inorganic/organic template (TiO_2-POEM)

Hybrid inorganic/organic templates (TiO_2-POEM) were synthesized according to the two-step synthetic ATRP method.[59] In the first step, 3.68 g of DMAP was mixed with 20 ml of MC and 2.8 ml of TEA at 0 ^oC with ice. Next, 4.8 ml of CPC in 20 ml of MC was added to the solution. Subsequently, 20.0 g of TiO_2 in 100 ml MC was added dropwise to the solution and then the solution was purged with nitrogen for 30 min. The mixture was stirred at room temperature for 24 h. After the reaction, the resulting solution was precipitated into methanol, and the product was separated by centrifuging. Finally, TiO_2-Cl nanoparticles were obtained and dried in a vacuum oven overnight at room temperature. In the second step, 8 ml of POEM was dissolved in 10 ml of DMSO. Next, 0.0264 g of CuCl and 0.072 ml of HMTETA were added to the solution, and 2 g of TiO_2-Cl nanoparticles were subsequently added. The solutions were purged with nitrogen for 30 min and the mixture was placed in a 90 ^oC oil bath for 24 h. After polymerization, the resulting solution was precipitated into methanol and the product was separated by centrifuging. The product was washed with methanol several times to remove impurities. Finally, TiO_2-POEM templates were obtained and dried in a vacuum oven overnight at room temperature.

Preparation of the bi-functional Nb-doped TiO_2/Ag ternary nanostructure photoanode

A FTO-coated conductive glass was sequentially cleaned in isopropanol and then in chloroform, and subsequently dried overnight in air before device fabrication. After the cleaning, the FTO glass was treated with a titanium(IV) bis (ethyl acetoacetato) diisopropoxide as a compact TiO_2 block layer, followed by heating to 450 ^oC for 2 h, holding for 30 min, and cooling to 30 ^oC for 8 h. Next, the bi-functional Nb-doped TiO_2/Ag ternary nanostructure solution was deposited onto the FTO glass using the doctor blade technique. In detail, the bi-functional Nb-doped TiO_2/Ag ternary nanostructure solution was prepared by a combination of selective reduction and a doping process. To begin, as-synthesized TiO_2-POEM templates (0.01 g) were dispersed in 1 ml of ethanol with 0.002 g of $AgCF_3SO_3$ for 2 h. After aging for 2 h, treatment of the resulting mixture

solution with heating to 50 °C for 3 h led to the selective reduction process of Ag^+ ions to Ag nanoparticles on the TiO_2-POEM templates. After that, 1 ml of ethanol solution containing 0.002ml of $Nb(OCH_2CH_3)_5$ was added into the selective reduction TiO_2-POEM/Ag solution for doping the Nb shell, and the reaction solution was then stirred for 12 h at room temperature in the dark. After casting the bi-functional Nb-doped TiO_2/Ag ternary nanostructure solution onto FTO glass, the photoanodes were aged at room temperature under 80% relative humidity for 30 h. Next, the prepared bi-functional Nb-doped TiO_2/Ag ternary nanostructure photoanodes-coated FTO glasses were sintered at 450 °C for 30 min, and cooled to 30 °C over 8 h. Subsequently, the bi-functional Nb-doped TiO_2/Ag ternary nanostructure was sensitized with the ruthenium solution 10^{-4} M in ethanol 50 °C for 2h in a dark room. Finally, the dye-sensitized solar cells photoanodes were immersed in absolute ethanol for 5 min to remove non-adsorbed dye on the surface. In addition, the pristine TiO_2 photo photoanodes (made from commercially available TiO_2 nanoparticles) Degussa P25 were used as a standard sample, according to previously reported procedures.[59,60]

Preparation of counter electrode

A FTO-coated conductive glass was used for a counter electrode. The glasses were cleaned by sonication in isopropanol and then in chloroform. The counter electrodes were fabricated by thermal depositing H_2PtCl_6 solution (4 wt% in isopropanol) onto the conductive FTO glass followed by thermal sintering at 450 °C for 30 min and cooling to 30 °C over 8 h.

Fabrication of DSSCs

Particular attention was paid to two types of electrolytes for the fabrication of DSSCs: 1) solid-state polymerized ionic liquid (PIL), i.e., poly(1-((4 ethenylphenyl)methyl)-3-butyl-imidazolium iodide) (PEBII); 2) liquid electrolyte consisting of 1-butyl-3-methylimidazolium iodide, iodine (I_2), guanidinium thiocyanate, and 4-tert-butylpyridine (TBP) in acetonitrile and valeronitrile. For the solid electrolyte DSSCs, an I_2-free PIL electrolyte solution in acetonitrile was directly cast onto the photoanode, according to previously reported procedures.[29,54] First, a 2 wt% dilute PIL electrolyte solution was cast onto a dye-adsorbed photoanode and evaporated very slowly for easy penetration of the electrolytes through the nanopores of the TiO_2 layer. Next, a 10 wt% PIL electrolyte solution was cast onto the photoanode and covered the counter electrode. Both electrodes were then superimposed and pressed between two glass plates to achieve slow evaporation of the solvent and a thin electrolyte layer. The cells were placed in a vacuum oven for one day for complete evaporation of the solvent. In the case of the liquid system, the photoanode and counter electrode were sealed together in a sandwich configuration using a hot-melt 60 μm thick Surlyn film. The inter-electrode space was filled with an electrolyte by a vacuum back-filling method. The holes were sealed using a small piece of hot-melt 60 μm thick Surlyn film and a microscope cover slip. Liquid electrolyte was composed of 0.6 M 1-butyl-3-methylimidazolium iodide, 0.03 M I_2, 0.1 M guanidinium thiocyanate, and 0.5 M 4-tert-butylpyridine in a mixture of acetonitrile and valeronitrile (v/v, 85:15).

Material characterization

Energy-filtering transmission electron microscopy (EF-TEM) pictures were obtained in order to observe the morphology of the photoanodes using a Philips CM30 microscope operating at 300 kV. For EF-TEM measurements, the dried films were dispersed in ethanol; next, a drop of this solution was placed onto a standard copper grid, followed by evaporation of the solvent in air. The X-ray diffraction (XRD) experiment was performed on a Rigaku 18 kw rotating anode X-ray generator, with Cu Ka radiation (λ = 1.5406 Å) operated at 40 kV and 300 mA. The 2θ range was from 5 ° to 60 °, with a scanning speed of 3 °/min, and the distance from the sample to the detector was 185 mm. Surface compositions of the photoanodes were investigated by X-ray photoelectron spectroscopy (XPS) using a VG Scientific ESCALAB 220 spectrometer equipped with a hemispherical energy analyzer. A nonmonochromatized Al K X-ray source (h = 1486.6 eV) was operated at 12.5 kV and 16 mA under analyzer chamber pressure less than 10^{-6} Pa. UV-visible spectroscopy was measured with a spectrophotometer (Hewlett Packard) in the range 200 to 800 nm. The photoanode thickness was measured by alpha-step IQ surface profile (KLA Tencor).

Solar cell characterization

Intensity modulated photocurrent/voltage spectroscopy (IMPS/IMVS) measurements were carried out on a electrochemical workstation equipped with a frequency response analyzer under a modulated red light emitting diode (635 nm) driven by a source supply, which can provide both DC and AC components of the illumination. The frequency range was set from 0.01 Hz to 10 MHz. The incident photo to current conversion efficiency (IPCE) spectra were measured with a spectral resolution of 5 nm using a 300 W xenon lamp and a monochromator equipped with order sorting filters (K3100). The IPCE value was calculated using the following equation:

$$IPCE = h\,c\,I / \lambda\,p \quad (13)$$

where h and c represent Planck's constant and the speed of light in a vacuum, respectively. I is the photocurrent density (mA/cm^2). λ and P are the wavelength (nm) and the intensity (mA/cm^2) of the incident monochromatic light, respectively. The current-voltage (I-V) characteristics of DSSCs were measured under illumination (AM1.5, 1 Sun) using a Keithley Model 2400 (1000 W xenon lamp, Oriel, 91193). A typical cell had an active area of ca. 0.16 cm^2 and was masked using an aperture of the same area during the I-V measurements. A correction for the spectral mismatch between the simulated light and natural sunlight was made against a certified reference Si solar cell (Fraunhofer Institute for Solar Energy System, Mono-Si + KG filter, Certificate No. C-ISE269) for a sunlight intensity of one (100 mW/cm^2). This calibration was verified with an NREL-calibrated Si solar cell (PV Measurements Inc.). The DSSCs temperature was maintained at 25 °C throughout the measurement time using a Peltier cooling apparatus. The photoelectrochemical performances were calculated by the following equations:

$$FF = V_{max} \cdot J_{max} / V_{oc} \cdot J_{sc} \quad (14)$$

$$\eta\ (\%) = V_{max} \cdot J_{max} \cdot 100 / P_{in} = V_{oc} \cdot J_{sc} \cdot FF \cdot 100 / P_{in} \quad (15)$$

where J_{sc} is a short-circuit current density (mA/cm^2), V_{oc} is an open-circuit voltage (V), P_{in} is an incident light power, FF is the fill factor, η is an overall energy conversion efficiency, and J_{max} (mA/cm^2) and V_{max} (V) are the current density and voltage in the J-V curve, respectively, at the point of maximum power output.

Acknowledgements

This work was supported by the Korea Center for Artificial Photosynthesis (KCAP) (2009-0093883), the Core Research Program (NRF-2012R1A2A2A02011268), and the Energy Efficiency & Resources of the Korea Institute of Energy Technology Evaluation and Planning (KETEP) (20122010100040), and Converged Energy Materials Research Center program of Defense Acquisition Program Administration and Agency for Defense Development.

Notes and references

[a] *Department of Chemical and Biomolecular Engineering,Yonsei University, 262 Seongsanno, Seodaemun-gu, Seoul 120-749, South Korea. Fax: +82-2-312-6401; Tel: +82-2-2123-7799; E-mail: jonghak@yonsei.ac.kr*

† Electronic Supplementary Information (ESI) available: [details of any supplementary information available should be included here]. See DOI: 10.1039/b000000x/

1 B. O'Regan and M. Gratzel, *Nature* 1991, **353**, 737.
2 M. McCune, W. Zhang and Y. Deng, *Nano Lett.* 2012, **12**, 3656.
3 J. Huang, O. Buyukcakir, M. W. Mara, A. Coskun, N. M. Dimitrijevic, G. Barin, O. Kokhan, A. B. Stickrath, R. Ruppert, D. M. Tiede, J. F. Stoddart, J.-P. Sauvage and L. X. Chen, *Angew. Chem. Int. Ed.* 2012, **51**, 12711.
4 D.H. Kim, M. Woodroof, K. Lee and G.N. Parsons, *ChemsusChem*, 2013, **6**, 1014.
5 J. T. Park, D. K. Roh, R. Patel, E. Kim, D. Y. Ryu and J. H. Kim, *J. Mater. Chem.* 2010, **20**, 8521.
6 D. G. Brown, P. A. Schauer, J. Borau-Garcia, B. R. Fancy and C. P. Berlinguette, *J. Am. Chem. Soc.* 2013, **135**, 1692.
7 M. Cheng, X. Yang, J. Li, F. Zhang and L. Sun, *ChemSusChem,* 2013, **6**, 70.
8 J. Mao, N. He, Z. Ning, Q. Zhang, F. Guo, L. Chen, W. Wu, J. Hua and H. Tian, *Angew. Chem. Int. Ed.* 2012, **51**, 9873.
9 C.-W. Kung, H.-W. Chen, C.-Y. Lin, K.-C. Huang, R. Vittal and K.-C. Ho, *ACS Nano*, 2012, **6**, 7016.
10 M. Wu and T. Ma, *ChemSusChem*, 2012, **5**, 1343.
11 X. Li, L. Liu, G. Liu, Y. Rong, Y. Yang, H. Wang, Z. Ku, M. Xu, C. Zhong and H. Han, *Adv. Funct. Mat.* 2013, **23**, 3344.
12 Y. Liu, J.R. Jennings and Q. Wang, DOI: 10.1002/cssc.201300238.
13 C. Law, S. C. Pathirana, X. Li, A. Y. Anderson, P. R. F. Barnes, A. Listorti, T. H. Ghaddar and B. C. O'Regan, *Adv. Mater.* 2010, **22**, 4505.
14 X. Lu, X. Mou, J. Wu, D. Zhang, L. Zhang, F. Huang, F. Xu and S. Huang, *Adv. Funct. Mater.* 2010, **20**, 509.
15 M. Yang, D. Kim, H. Jha, K. Lee, J. Paul and P. Schmuki, *Chem. Commun.* 2011, **47**, 2032.
16 E. Barea, X. Xu, V. Gonzalez-Pedro, T. Ripolles-Sanchis, F. Fabregat-Santiago and J. Bisquerta, *Energy Environ. Sci.* 2011, **4**, 3414.
17 T. Nikolay, L. Larina, O. Shevaleevskiy and B. T. Ahn, *Energy Environ. Sci.* 2011, **4**, 1480.
18 M. D. Brown, T. Suteewong, R. S. S. Kumar, V. D'Innocenzo, A. Petrozza, M. M. Lee, U. Wiesner and H. J. Snaith, *Nano Lett.* 2011, **11**, 438.
19 J. Qi, X. Dang, P. T. Hammond and A. M. Belcher, *ACS Nano*, 2011, **5**, 7108.
20 H. Choi, W. T. Chen and P. V. Kamat, *ACS Nano*, 2012, **6**, 4418.
21 J. Du, J. Qi, D. Wang and Z. Tang, *Energy Environ. Sci.*, 2012, **5**, 6914.
22 S. D. Standridge, G. C. Schatz and J. T. Hupp, *J. Am. Chem. Soc.* 2009, **131**, 8407.
23 X. Dang, J. Qi, M. T. Klug, P.-Y. Chen, D. S. Yun, N. X. Fang, P. T. Hammond and A. M. Belcher, *Nano Lett.* 2013, **13**, 637.
24 T. Kawawaki, Y. Takahashi and T. Tatsuma, *Nanoscale*, 2011, **3**, 2865.
25 A. Yella, H.-W. Lee, H. N. Tsao, C. Yi, A. K. Chandiran, M. K. Nazeeruddin, E. W-G. Diau, C. Y. Yeh, S. M. Zakeeruddin and M. Gratzel, *Science*, 2011, **334**, 629.
26 I. Chung, B. Lee, J. He, R. P. H. Chang and M. G. Kanatzidis, *Nature*, 2012, **485**, 486.
27 M. M. Lee, J. Teuscher, T. Miyasaka, T. N. Murakami and H. J. Snaith, *Science*, 2012, **338**, 643.
28 H.-S. Kim, C.-R. Lee, J.-H. Im, K.-B. Lee, T. Moehl, A. Marchioro, S.-J. Moon, R. Humphry-Baker, J.-H. Yum, J. E. Moser, M. Gratzel and N.-G. Park, *Sci. Rep.* 2012, **2**, 591.
29 S. H. Ahn, W. S. Chi, D. J. Kim and J. H. Kim, *Adv. Funct. Mater.* 2013, **23**, 3901.
30 W. S. Chi, D. K. Roh, S. J. Kim, S. Y. Heo and J. H. Kim, *Nanoscale*, 2013, **5**, 5341.
31 N. C. Jeong, C. Prasittichai, and J. T. Hupp, *Langmuir* 2011, **27**, 14609.
32 X. Lü, F. Huang, X. Mou, Y. Wang and F. Xu, *Adv. Mater.* 2010, **22**, 3719.
33 K. Tennakone, P.V.V. Jayaweera and P.K.M. Bandaranayake, *J. Photochem. Photobio. A: Chem.* 2003, **158**, 125.
34 T. Kawawaki, Y. Takahashi and T. Tatsuma, *Nanoscale* 2011, **3**, 2865.
35 J.T. Park, J.H. Koh, J.K. Koh and J.H. Kim, *Appl. Surf. Sci.* 2009, **255**, 3739.
36 A. Ghicov, S. Aldabergenova, H. Tsuchyia and P. Schmuki, *Angew. Chem., Int. Ed.* 2006, **45**, 6993.
37 J.T. Park, K.J. Lee, M.-S. Kang, Y.S. Kang and J.H. Kim, *J. App. Pol. Sci.* 2007, **106**, 4083.
38 S. G. Chen, S. Chappel, Y. Diamant and A. Zaban, *Chem. Mater.* 2001, **13**, 4629.
39 Y. Wang, B. M. Smarsly and I. Djerdj, *Chem. Mater.* 2010, **22**, 6624.
40 E. Tang, H. Liu, L. Sun, E. Zheng and G. Cheng, *Eur. Polym. J.* 2007, **43**, 4210.
41 L.E.J. Brus, *Chem. Phys.* 1983, **79**, 5566.
42 L.M. Peter, *Phys. Chem. Chem. Phys.* 2007, **9**, 2630.
43 J.T. Park, J.H. Koh, J.A. Seo, Y.S. Cho and J.H. Kim, *App. Sur. Sci.* 2011, **257,** 8301.
44 J.T. Park, J.H. Koh, J.A. Seo, D.K. Roh and J.H. Kim, *Macromol. Research*, 2009, **17**, 301.
45 K.L. Kelly, E. Coronado, L.L. Zhao and G.C. Schatz, *J. Phys. Chem. B* 2003, **107**, 668.
46 K. Zhu, N. R. Neale, A. Miedaner and A. J. Frank, *Nano Lett.* 2007, **7**, 69.
47 P. R. F. Barnes, L. Liu, X. Li, A. Y. Anderson, H. Kisserwan, T.H. Ghaddar, J.R. Durrant and B.C. O'Regan, *Nano Lett.* 2009, **9**, 3532.
48 J. v. d. Lagemaat and A.J. Frank, *J. Phys. Chem. B* 2001, **105**, 11194.
49 Q. Wang, J.E. Moser, M. Gratzel, *J. Phys. Chem. B* 2005, **109**, 14945.
50 A. Hagfeldt, G. Boschloo, L.C. Sun, L. Kloo and H. Pettersson, *Chem. Rev.* 2010, **110**, 6595.
51 B. M. Reinhard, M. Siu, H. Agarwal, A. P. Alivisatos and J. Liphardt, *Nano Lett.* 2005, **5**, 2246.
52 B. Ding, B. J. Lee, M. Yang, H. S. Jung and J.-K. Lee, *Adv. Energy Mater.* 2011, **1**, 415.
53 S. G. Kim, M. J. Ju, I. T. Choi, W. S. Choi, H.-J. Choi, J.-B. Baek and H. K. Kim, *RSC Adv.*, 2013, **3**, 16380.
54 Q. Li, J. Zhao, B. Sun, B. Lin, L. Qiu, Y. Zhang, X. Chen, J. Lu and F. Yan, *Adv. Mater.* 2012, **24**, 945.
55 Q. Li, X. Chen, J. Zhao, L. Qiu, Y. Zhang, B. Sun and F. Yan, *J. Mater. Chem.* 2012, **22**, 6674.
56 G. Wang, L. Wang, S. Zhuo, S. Fang and Y. Lin, *Chem. Commun.* 2011, **47**, 2700.
57 J.T. Park, J.H. Prosser, D.J. Kim and J.H. Kim, D. Lee, *ChemSusChem*, 2013, **6**, 856.
58 J.T. Park, W. S. Chi, D.K. Roh, S.H. Ahn and J.H. Kim, *Adv. Funct. Mater.* 2013, **23**, 26.

59 J.T. Park, J.H. Koh, J.A. Seo and J.H. Kim, *J. Mater. Chem.* 2011, **21**, 17872.
60 J.T. Park, R. Patel, H. Jeon, D.J. Kim, J.-S. Shin and J.H. Kim, *J. Mater. Chem.* 2012, **22**, 6131.

A table of content

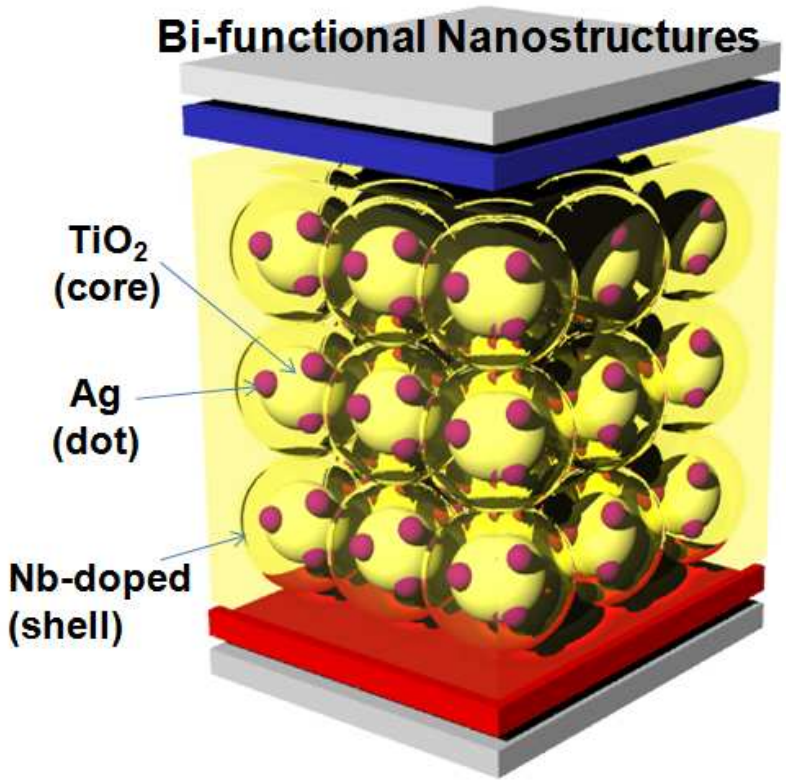

Bi-functional Nb-doped TiO_2/Ag ternary nanostructures were generated *via* subsequent ATRP, selective reduction and a doping process for dye-sensitized solar cells.